



The American Society of
Mechanical Engineers

Reprinted From
AMD-Vol. 174, Fluid Mechanics Phenomena in Microgravity
Editors: Dennis A. Siginer, R. L. Thompson, and L. M. Trefethen
Book No. H00869 - 1993

TRANSITION TO CHAOS IN THE PHYSICAL VAPOR TRANSPORT PROCESS - I

7N-27-TM

027671

Walter M. B. Duval
Materials Division
Processing Science and Technology Branch
NASA Lewis Research Center
Cleveland, Ohio

ABSTRACT

The global bifurcation of flow field structures is examined to determine its route to chaos. These flows occur during the physical vapor transport process for crystal growth. We use direct numerical simulation and cover the Rayleigh number range $0 < Ra_T \leq 5.03 \times 10^7$. The bifurcation diagram of the process indicates that there are four regions with distinct flow field structures, and three bifurcation events for a subrange $0 < Ra_T \leq 4.05 \times 10^6$. These regions have distinct dynamical characteristics as well. The flow field bifurcates from one region to another through selforganization into various cellular structures. The sequence of events in the flow field structure in each region shows a transition from a unidirectional advective-diffusive flow to two cells, subsequently to four cells, and finally to six cells. The dynamical characteristics of the process show that the first bifurcation event gives birth to a stable spiral cycle. The trajectory of the spiral cycle approaches a point attractor. The second bifurcation gives rise to a primary Hopf bifurcation; it connects a stationary state to a periodic state, hence a limit cycle results. The third bifurcation gives birth to a two frequency torus, also known as a secondary Hopf bifurcation. The route to chaos is via the two frequency torus bifurcation as proposed by Newhouse, Ruelle, and Takens.

1. INTRODUCTION

We investigate the global bifurcation of flow field structures in the physical vapor transport process via direct numerical simulation. The flow field structures are computed for a range of parameters spanning low gravity to ground based conditions. Through the construction of a bifurcation diagram, we trace various bifurcations to establish the route to chaos. For each transition region of the bifurcation diagram, we deduce qualitatively from bifurcation and stability analysis the mechanisms through which stability is lost. Transition of the flow field from steady, periodic, quasi-periodic, and chaos is quantified through time histories, phase space trajectories, and power spectra.

The physical vapor transport process (an example of a dissipative dynamical system) is used to grow single crystals for device applications. This process involves sublimation of a material from a hot source and condensation to a cool sink where the crystal is formed. During transport an inert gaseous component is also present which is rejected at the interface. For practical reasons this process is carried out in the vertical configuration in which the bottom is hotter than the top. This is similar to the Rayleigh-Benard process, except for fluxes at the boundaries. In our research, the source material of interest is mercurous chloride. This material has attractive properties for device applications, and

it is used in acousto-optic opto-electronic devices such as Bragg cells, x-ray detectors, wideband spectroscopic devices, and acousto-optic tunable filters.

Dissipative dynamical systems are known to exhibit a rich variety of spatial patterns stemming from their inherent nonlinearity. These spatial patterns are functions of parameters which govern the extent to which the system deviates from thermodynamic equilibrium¹. A few notable examples are the Rayleigh-Benard, double-diffusive systems, and reaction-diffusion processes in liquid mixtures. The spatial patterns of the Rayleigh-Benard convection have been studied recently both experimentally² and numerically³. Because these systems are governed by nonlinear coupled partial differential equations, solutions for a parametric range is difficult. Approximations are the usual recourse; one such approximation is through linear stability analysis which is quite useful for establishing stability boundaries. Because of the inherent nature of this approximation, it establishes the first bifurcation point. Beyond the first bifurcation point, the nonlinearity of the system becomes important and recourse has to be made to the solution of the coupled equations. Another approximation technique that has yielded much insight into the solution of these systems, is truncation of the nonlinear equations. The success of this approach is epitomized in the Lorenz system of equations⁴. In this approach, a coupled system of nonlinear partial differential equations (the Rayleigh-Benard system) is successfully reduced to a system of coupled ordinary differential equations⁵. The advantage of this approach is that it allows the physics of the problem to be studied more easily than with the full set of equations. Solutions can be obtained for a wide range of parameters, and the results can be displayed succinctly on a bifurcation diagram. Numerical techniques can be employed such as continuation methods^{6,7} to construct bifurcation diagrams for the entire parametric space. Unfortunately, as pointed out by Marek & Kubiček⁷, these techniques are not applicable to coupled nonlinear partial differential equations with more than one spatial coordinate, and the theory for these systems is still in development. It is therefore necessary to solve the entire system of equations to construct the bifurcation diagram in order to obtain insight into the nonlinear regime.

The purpose of this work is to analyze the physical vapor transport process from a dynamical systems point of view and investigate its route to chaos. To that end, we solve the full time dependent nonlinear coupled equations numerically, and construct a bifurcation diagram to show its distinct bifurcations on its route to chaos. The parametric range considered falls within practical

conditions for crystal growth systems. Dissipative dynamical systems are known to exhibit many different routes to chaos (Verlade⁸). Among these routes are period doubling (subharmonics), intermittency, and quasi-periodicity. We show that four distinct flow field regions, each with its own structure, separated by three bifurcation events occur in our system on its way to chaos. In the first region, however slight the deviation from thermodynamic equilibrium, there always exist a base flow stemming from the advective-diffusive flux which is stable. The time history of the flow field shows that it approaches a point attractor asymptotically. This is in contrast to the Rayleigh-Bernard system which has a quiescent state. At the first bifurcation event, this flow selforganizes into two cells. In the second region, the dynamics of the flow field show that there is a birth of a spiral in which a point attractor is approached. At the second bifurcation event, there is a standard Hopf bifurcation; the flow field selforganizes into four cells. This is accompanied by the birth of a limit cycle. In the third bifurcation, there is an exchange of stability from a limit cycle to a two frequency torus which exhibits quasi-periodicity. This is also known as a secondary Hopf bifurcation. There are six cells in this region. The route to chaos stems from the two frequency torus bifurcation which has been proposed by Newhouse, Ruelle, and Takens⁹.

This paper is organized as follows. We describe the physics of the physical vapor transport process and its mathematical description. We establish the parametric space of interest. We construct a bifurcation diagram for practical crystal growth parametric range. We deduce qualitatively the mechanisms by which local stability is lost from bifurcation and stability theory. We quantify thoroughly each flow field region through its time histories, phase space trajectories, and power spectra. And finally we discuss the relevance if this work to practical crystal growth by the physical vapor transport process.

2. MATHEMATICAL FORMULATION

The basis of the physical vapor transport process, as shown in Figure 1, consists of sublimation from the source material and condensation at the crystal region to form a single crystal. The vapor component is transported with the presence of an inert component. This inert component is either intentionally added or results from outgassing from container walls or impurities in the source material. Thus inherently there is always a second component present in the system, however small. This inert component is assumed to be rejected at the interface, and there is no dissocia-

tion of the vapor crystal component. This process can be controlled through either the temperature difference between the source and crystal as well as intentional addition of a known partial pressure of an inert component, typically argon¹⁰. This process occurs at constant total pressure¹¹. Typical partial pressure profiles are also shown in Figure 1 to illustrate trends; for the crystal component, the trends are shown with solid lines. For a fixed source temperature, the process can be controlled by increasing or decreasing the temperature at the crystal region. The corresponding partial pressure trends of the crystal component as the temperature difference increases are illustrated with P'_{A_c} and P_{A_c} respectively. The trends for the inert component follow similarly.

For the mathematical description of the problem, consider a vertical enclosure in which the source is at the bottom and the crystal at the top. This corresponds to the configuration of interest for crystal growth of mercurous chloride. In the configuration of interest, the y coordinate has its origin at the source vapor boundary and ends at the crystal vapor boundary. The height and width of the cavity are H and L respectively. Let \vec{n} be the normal to the inside enclosure, $\vec{\tau}$ its tangent, and Γ its boundary. The source and crystal move so slowly in comparison to the vapor that their effects are assumed negligible, only the vapor region is considered. The velocity in the vapor region corresponds to the mass average velocity. We assume thermodynamic equilibrium at the interfaces, thus the mass fractions are fixed. For an incompressible Boussinesq fluid, the governing equations (* denotes dimensional variables) comprising of continuity, momentum, energy, and species may be stated as follow:

$$\nabla \cdot \vec{V}^* = 0 \quad (1)$$

$$\bar{\rho} \frac{D\vec{V}^*}{Dt} = -\nabla p^* + \bar{\mu} \nabla^2 \vec{V}^* + \rho \vec{x}^* \quad (2)$$

$$\frac{DT^*}{Dt} = \alpha \nabla^2 T^* \quad (3)$$

$$\frac{D\omega_A^*}{Dt} = \bar{D}_{AB} \nabla^2 \omega_A^* \quad (4)$$

where

$$\rho = \bar{\rho}(1 - \beta \Delta T + \gamma \Delta \omega)$$

$$\beta = -\frac{1}{\bar{p}} \left(\frac{\partial p}{\partial T} \right)_{\omega_A}$$

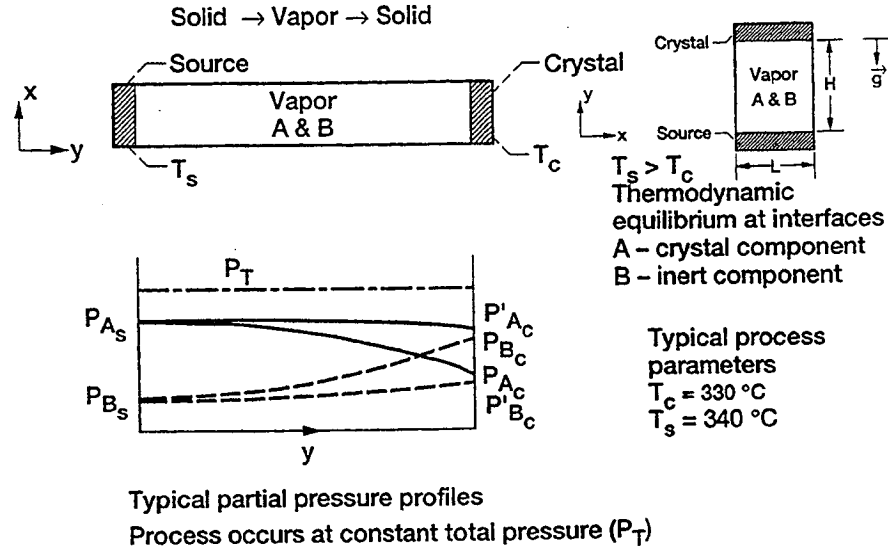


Figure 1. Basis of the Physical Vapor Transport process

$$\gamma = \frac{1}{\rho} \frac{\partial \rho}{\partial \omega} \tau$$

$$\vec{r} = \epsilon_{Rn} \vec{j}$$

The initial and boundary conditions are:

Initial conditions:

$$t = 0 \quad 0 < x^* < L, \quad 0 < y^* < H$$

$$T^*(x^*, y^*, 0) = T_S^* + (y^*/H) (T_C - T_S)$$

$$\omega_A^*(x^*, y^*, 0) = \omega_{AS}^* + (y^*/H) (\omega_{AC} - \omega_{AS})$$

Boundary conditions:

No slip at the left and right walls,

$$t > 0 \quad \vec{v} \cdot \vec{n} = 0, \quad x^* = 0, \quad x^* = H, \quad \vec{v} \cdot \vec{y}$$

Prescribed temperature and fixed mass fraction at the source and crystal boundary,

$$T^*(x^*, 0, t^*) = T_S, \quad \omega_A^*(x^*, 0, t^*) = \omega_{AS}, \quad y^* = 0, \quad \vec{v} \cdot \vec{x}$$

$$T^*(x^*, H, t^*) = T_C, \quad \omega_A^*(x^*, H, t^*) = \omega_{AC}, \quad y^* = H, \quad \vec{v} \cdot \vec{x}$$

Insulated and impermeable boundaries at left and right walls,

$$\nabla T^* \cdot \vec{n} = 0, \quad \nabla \omega_A^* \cdot \vec{n} = 0 \quad \text{on } \Gamma \quad \text{at } x^* = 0, \quad x^* = L, \quad \vec{v} \cdot \vec{y}$$

Sublimation and condensation at the boundary of the source and crystal,

$$\vec{v} \cdot \vec{n} = - \frac{\bar{D}_{AB}}{1 - \omega_A^*(x^*, 0, t^*)} (\nabla \omega_A^* \cdot \vec{n}), \quad \text{at } y^* = 0, \quad y^* = H, \quad \vec{v} \cdot \vec{x}$$

with vanishing tangential velocity at the interface,

$$\vec{v} \cdot \vec{\tau} = 0 \quad \text{on } \Gamma \quad \text{at } y^* = 0, \quad y^* = H, \quad \vec{v} \cdot \vec{x}$$

In the above governing equations the transport coefficients are estimated from molecular theory using Chapman-Enskog's formulas¹². The condition for sublimation and condensation has been derived by Westphal & Rosenberger¹³, and its applicability to crystal growth has been discussed by Rosenberger & Muller¹⁴. The gas mixture is assumed to be ideal. It can be shown that,

$$\beta = 1/\bar{T} \quad (4a) \quad \text{and} \quad \gamma = \frac{M_A - M_B}{\omega_A^*(M_B - M_A) + M_A} \quad (4b) \quad (4)$$

where

$$\omega_A^* = \frac{1}{1 + (P_T/P_A - 1) M_B/M_A} \quad (5)$$

using the mass fraction and mole fraction relations¹². P_T is the total pressure and is related to the partial pressures by $(P_T = P_A + P_B)$. P_A is known for mercurous chloride, thus the corresponding mass fraction at the interfaces can be calculated. This is fixed by the thermodynamics of the process.

For the problem at hand, we are interested in diffusive-convective physical vapor transport with the presence of impurities. This is modeled by assuming $M_A = M_B$, this implies $\gamma = 0$; thus the solutal Rayleigh number also vanishes. The excess pressure of the second component affects the binary diffusion coefficient which determines the advective-diffusive flux at the boundary. Since D_{AB} is proportional to $1/P_T$, as the level of impurity increases the advective-diffusive flux decreases, in the limit this problem approaches the Rayleigh-Benard problem. Note also that as $P_B \rightarrow 0$, the binary diffusion coefficient approaches the self-diffusion coefficient of a single fluid.

2.1 Scaling

The above equations are transformed into vorticity-stream function relations for computation. The characteristic length, time, and velocity (U_c) are scaled as H , H^2/α , and αH respectively. The mass fraction and temperature are normalized as $\omega_A = (\omega_A^* - \omega_{AC}^*)/(\omega_{AS}^* - \omega_{AC}^*)$, and $T = (T^* - T_C^*)/(T_S^* - T_C^*)$, respectively. ΔT and $\Delta \omega$ equal $(T_S^* - T_C^*)$ and $(\omega_{AS}^* - \omega_{AC}^*)$, respectively. Let,

$$u^* = \frac{\partial \Psi^*}{\partial y^*} \quad v^* = -\frac{\partial \Psi^*}{\partial x^*} \quad \zeta^* = \frac{\partial v^*}{\partial x^*} - \frac{\partial u^*}{\partial y^*}$$

The dimensionless scaled equations become:

$$Ar^2 \frac{\partial^2 \Psi}{\partial x^2} + \frac{\partial^2 \Psi}{\partial y^2} = -\zeta \quad (7)$$

$$\frac{1}{Pr} \frac{\partial \zeta}{\partial t} + \frac{1}{Pr} \left[Ar u \frac{\partial \zeta}{\partial x} + v \frac{\partial \zeta}{\partial y} \right] = \left[Ar^2 \frac{\partial^2 \zeta}{\partial x^2} + \frac{\partial^2 \zeta}{\partial y^2} \right] + Ra_T Ar \frac{\partial T}{\partial x} \quad (8)$$

$$\frac{\partial T}{\partial t} + \left[Ar u \frac{\partial T}{\partial x} + v \frac{\partial T}{\partial y} \right] = \left[Ar^2 \frac{\partial^2 T}{\partial x^2} + \frac{\partial^2 T}{\partial y^2} \right] \quad (9)$$

$$\frac{\partial \omega_A}{\partial t} + \left[Ar u \frac{\partial \omega_A}{\partial x} + v \frac{\partial \omega_A}{\partial y} \right] = \frac{1}{Le} \left[Ar^2 \frac{\partial^2 \omega_A}{\partial x^2} + \frac{\partial^2 \omega_A}{\partial y^2} \right] \quad (10)$$

The conditions for sublimation and condensation at the boundaries become:

$$v(x, 0, t) = -\frac{1}{Pe} \frac{\Delta \omega}{(1 - \omega_{AS})} \frac{\partial \omega_{AS}}{\partial y}$$

$$v(x, 1, t) = -\frac{1}{Pe} \frac{\Delta \omega}{(1 - \omega_{AC})} \frac{\partial \omega_{AC}}{\partial y}$$

The dimensionless parameters are:

$$Ar = \frac{H}{L} \quad Ra_T = \frac{\beta \Delta T \epsilon_{Rn} H^3}{\nu \alpha} \quad Pe = \frac{U_0 H}{\bar{D}_{AB}}$$

$$Pr = \frac{\bar{\nu}}{\alpha} \quad Le = \frac{\alpha}{\bar{D}_{AB}}$$

Let Λ be the vector space of the independent parameters. Thus $\Lambda = \Lambda(Ra_T, Ar, Pe, Pr, Le)$ is a vector space with five independent parameters. These parameters are respectively, the Rayleigh number, the aspect ratio, the Peclet, Prandtl, and Lewis numbers. The entire dynamical process can be quantified by studying the effects of these parameters on the dynamics of the flow field. Note that the problem has two characteristic velocities, U_c and U_0 . They represent components from convection (U_c) which is dependent on buoyancy, and the advective-diffusive flux (U_0) at the interfaces which is dependent on the thermodynamics. These two variables are independent of each other. U_0 can be estimated by relating the Peclet number to the thermodynamic variables; this prescribes the Peclet number. This is given by

$$Pe = \ln(P_B(H)/P_B(0)). \quad (11)$$

These equations are solved using finite difference techniques, see¹⁵ for details. We use a 60x60 grid size for all of our computations. The choice of this grid size is adequate to resolve the details of the flow field and did not affect the number of cells in the flow or resolution of the structures.

3. Results and Discussion

3.1 Parametric Space Variation

The construction of bifurcation diagrams to study variation of five independent parameters ($\Lambda = \Lambda(Ra_T, Ar, Pe, Pr, Le)$) represents a formidable computational task. We restricted the number of parametric variations by considering the most important variations that occur experimentally for a given crystal growth system. For a given crystal growth condition we selected argon as an inert gas to represent the impurity component at a fixed partial pressure of 10 Torr. Other than effects of temperature variations, this fixes the range on the Peclet number. Since we are considering a specific system, mercurous chloride, the range for Pr and Le numbers is also fixed. These three parameters can be seen as passive in the parametric variation. Since we are interested in the growth of large bulk single crystals, the cavity size considered is 5 cm by 5 cm, unless otherwise specified the aspect ratio is fixed at 1. The aspect ratio is varied to show its effect on flow stability; however, this is limited to a fixed crystal growth condition, i.e. $\Delta T = 10^\circ K$. Given a cavity with a certain aspect ratio, the experi-

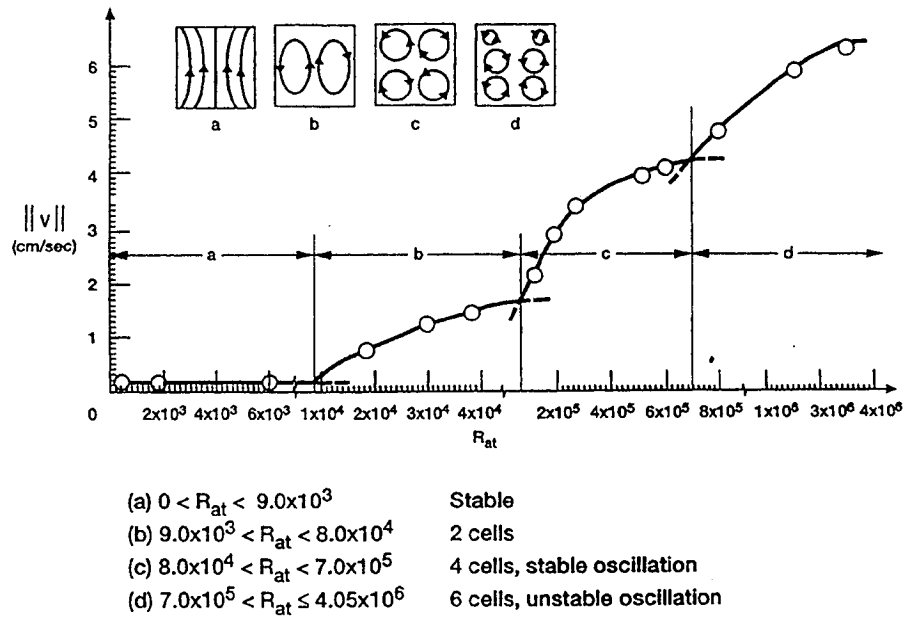


Figure 2. Bifurcation diagram for $Ar=1$ and $0 < Ra_T \leq 4.05 \times 10^6$

mentalist is free to vary the temperature difference between the source and crystal to achieve various growth conditions. This translates to variation of the Rayleigh number. In this light, we investigate thoroughly the effect of variation of the Rayleigh number on the fluid dynamic behavior. This effectively reduces our parametric variation to a single parameter ($\Lambda = \Lambda(Ra_T)$), the Rayleigh number. A few selected parameters are shown in Table 1. These conditions range from low gravity environment aboard a Space Shuttle to ground based conditions in a laboratory.

In Table 1 the thermophysical properties required for the dimensionless numbers are calculated at the average temperature. The variation in the Prandtl and Lewis numbers stem from variation in the thermophysical properties due to temperature. Similarly the range in the Peclet number is due to effects of thermodynamic conditions on temperature. Thus the effects of these dimensionless parameters are passive in the parametric variation as compared to the Rayleigh number.

TABLE 1 - PARAMETRIC RANGE

Case	ϵ	Ra_T	Pr	Le	Pe
1	1	3.02×10^4	.815	.408	.748
2	1	3.83×10^4	.871	.411	.876
3	1	1.08×10^5	.848	.427	1.54
5	1	2.66×10^5	.814	.453	2.18
6	1	6.10×10^5	.773	.487	2.76
7	1×10^{-2}	6.10×10^3	.773	.487	2.76
8	1	7.45×10^5	.763	.496	2.90
9	1	8.19×10^5	.758	.500	2.96
10	1	1.28×10^6	.736	.521	3.25
11	1	1.92×10^6	.717	.540	3.50
12	1×10^{-5}	1.92×10^1	.717	.540	3.50
13	1×10^{-6}	1.92×10^0	.717	.540	3.50
14	1×10^{-7}	1.92×10^{-1}	.717	.540	3.50
15	1	4.05×10^6	.686	.572	3.93
16	1	8.03×10^6	.663	.598	4.30
17	1	1.53×10^7	.646	.618	4.63
18	1	2.81×10^7	.633	.633	4.94
19	1	5.03×10^7	.623	.645	5.23

3.2 Bifurcation Diagram

The bifurcation diagram resulting from varying the Rayleigh number is shown in Figure 2. The ordinate corresponds to the asymptotic maximum magnitude of the flow field. We selected to keep a linear scale on the abscissa in order to show the functional relationship of the velocity on the Rayleigh number. There exists four distinct regions illustrating the path from steady advective-diffusive flow to chaos. Each region has its own particular flow field structure. As the Rayleigh number is increased three distinct bifurcations occur. During the first bifurcation from *a* to *b* there is an exchange of stability from a steady flow to selforganization of the flow field to two cells. This is similar to the first bifurcation in the Rayleigh-Bernard problem which results from growth of monotonic disturbances. However, the Rayleigh-Bernard bifurcation occurs from a quiescent state. In the second bifurcation from *b* to *c* there is transition from two cells to four cells. This bifurcation gives birth to a limit cycle, known as the Hopf bifurcation. Note that in region *c* the velocity increases like the square root of the Rayleigh number; this is a principal property in the neighborhood of a Hopf bifurcation. The third bifurcation from *c* to *d* results in the transition to six cells. This yields, as will be shown, to a two frequency torus, also known as a secondary Hopf bifurcation. A new frequency component arises which is incommensurate with the prior frequency from the limit cycle. These two frequency components form an irrational fraction; in this case the flow is quasi-periodic. This route to chaos via bifurcation to a two frequency torus corresponds to the scenario proposed by Newhouse, Ruelle, Takens⁹. In region *d*, further increase in the Rayleigh number leads to chaos. This is indicated, as will be shown, by a thick chaotic limit set in the phase space trajectory and a broadband power spectrum. In the following we describe the fluid dynamic structure in detail. We show the effect of the aspect ratio on stability of the flow field. For each region of the bifurcation diagram we discuss qualitatively its local bifurcation, the mechanisms by which stability is lost, and we quantify each region of the flow based on its time histories, phase space trajectories, and power spectra.

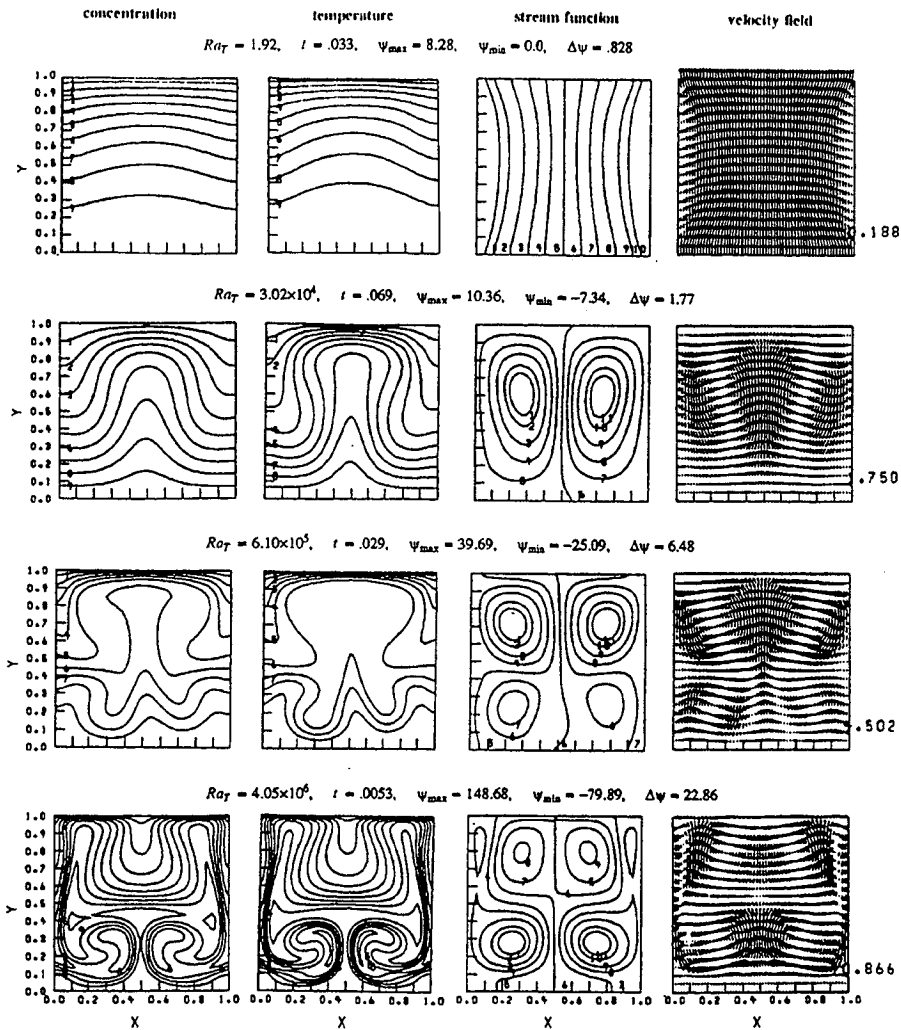


Figure 3. Structures of field variables corresponding to the four regions in the bifurcation diagram.

3.3 Flow Field Characteristics for Regions a-d

The flow field characteristics, corresponding to regions a-d on the bifurcation diagram for representative Rayleigh numbers are shown in Figure 3. We show contours of the scalar components, concentration and temperature. The structure of the flow field is illustrated with contours of the stream function and the direction of the flow with velocity vectors. The stream function is divided into ten intervals, $\Psi_{\min} = \Psi_1$, $\Psi_{\max} = \Psi_{11}$, and the maximum of the vector field is indicated on the right hand corner of the vector field plot and it is scaled as $V_{\max}/8 = \text{cm/sec}$. For a particular case in region a ($Ra_T = 1.92$) the flow is advective-diffusive, it is unidirectional with a parabolic velocity profile. Since the Lewis number does not equal one, the scalar components do not diffuse at the same rate. The deviation of the scalar components from its initial conduction state is small. This condition corresponds to a typical situation that would occur in low gravity. And it also represents the best mode for growing crystals because the flow is steady and the gradients in concentration and temperature are uniform at the crystal interface. Note that for the low gravity conditions, see Table 1 cases 12-14, the Rayleigh number was varied through the g-level so that it would become less than the Peclet number. The results show that the asymptotic velocity field is equal for all three cases. Thus at a certain g-level or corresponding Rayleigh number, as shown on the bifurcation diagram, there is no

change in the asymptotic state of the velocity field. In region b ($Ra_T = 3.02 \times 10^4$), after the first bifurcation, the base advective-diffusive flow selforganizes into two cells. This flow field gives rise to plumes as shown in the concentration and temperature field. Oscillations that occur in this region are damped and an invariant steady state flow structure exists. Because a steady state exists in this region, good quality crystals can be grown, however precautionary measures should be taken. The bifurcation from region b to c ($Ra_T = 6.10 \times 10^5$) leads to four cells, even though detailed studies¹⁵ of the global dynamics of the flow field show that it approaches an invariant flow structure, the oscillations are not damped; they proceed forever. In region d ($Ra_T = 4.05 \times 10^6$) the flow field bifurcates to six cells. The strength of convection increases by two fold. The intensity of the convective flow field causes the formation of counter propagating plumes from the top and bottom of the cavity. The long time asymptotic state is no longer periodic, the flow has become aperiodic. For high quality crystal growth regions c and d should be avoided.

3.4 Global Dynamics of The Flow Field

Two types of flows prevail for the range of Rayleigh numbers considered, core driven and boundary layer driven flows. We illustrate the typical dynamics of the flow field as time increases for a fixed Rayleigh number for these flows. In Figure 4 $Ra_T = 3.83 \times 10^4$, for the core driven flow, we show the typical evolu-

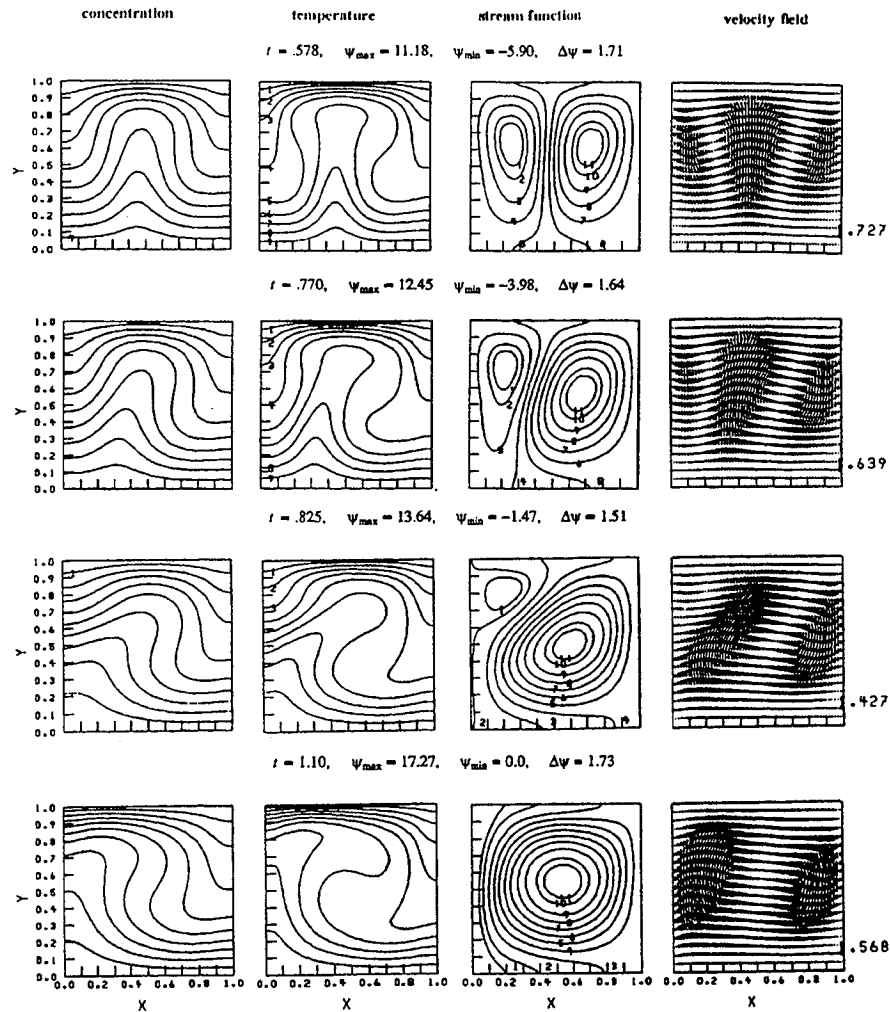


Figure 4. Transition to steady state for a core driven flow, $Ra_T = 3.73 \times 10^4$,
 $Pe = .876$, $Pr = .871$, $Le = .411$

tion toward an invariant flow structure. The evolution of the flow field gives rise to a plume, $t = .578$. At $t = .77$, there is a loss of symmetry; the right cell grows. This growth continues until there is an invariant structure comprised of a single cell at the right hand side and uniform flow on the left hand side of the cavity. The overall trend of this flow is clockwise. This structure is similar to a result shown by Shvartsblat¹⁶ for a related problem. Note that for other cases examined, see Table 1, the invariant structure is a counterclockwise flow. The directionality of the invariant structure of the flow field have equal probabilities in terms of the sense of rotation. This is similar to the Rayleigh-Benard system which also shows equal probability in the sense of rotation of the cells. This case shows that the dynamics of the flow evolve to an invariant structure which is steady. However, for Rayleigh numbers in region c, the invariant structure pulsates because of oscillation in the flow.

Another case of interest is the boundary layer driven flows. An illustration is shown in Figure 5 for $Ra_T = 1.53 \times 10^7$. In this case we show the evolution of the flow field. Initially there is an intensive flow at the side walls. This is in contrast to the core driven flow where the initial changes in the scalar components occur in the middle of the cavity. This intensive flow leads to the formation of four cells, $t = .0011$. Two counter rotating cells are formed near the top boundary which reverses the direction of the top

plume. This occurs because the flow is so strong that it stagnates at the top boundary, thus forming a counter rotating flow. The flow field subsequently evolves to six cells, $t = .0015$, in which there are two counter propagating plumes from the top and bottom of the cavity. As time increases, further bifurcation of the flow field structure occurs, such as growth and amalgamation of cells and oscillations of the flow field structure.

3.5 Effect of Aspect Ratio

To discern the effect of the aspect ratio on the bifurcation diagram in Figure 2, it would be necessary to construct an independent bifurcation diagram for each aspect ratio of interest. Since this is not our intended purpose, we will simply fix the Rayleigh number threshold through the temperature difference ($\Delta T = 10^\circ K$, which corresponds to case 5), and vary H and L sequentially to approach both a horizontal narrow cavity as well as a vertical one. We show the aspect ratio and its corresponding Rayleigh number in Table 2. $Ar = 5$ represents the vertical narrow cavity, whereas $Ar = 1/5$ represents the horizontal narrow cavity. The result for this parametric variation is shown in Figure 6. Note that the maximum velocity occurs for the square cavity. As we approach the vertical narrow cavity $Ar = 5$ the velocity decreases slowly and the flow field becomes stable. This corresponds to the advective-diffusive flow of region a on the bifurcation diagram. This shows that wall effects, because they introduce viscous drag

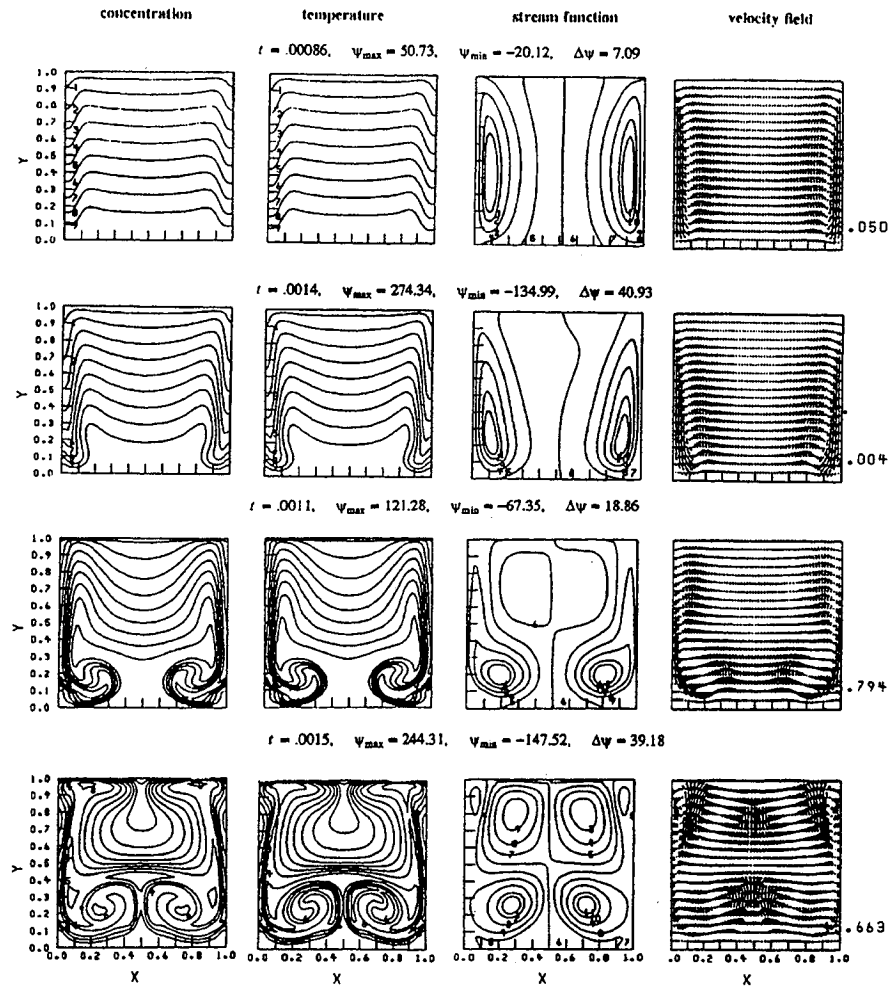


Figure 5. Evolution of the flow field for a boundary layer driven flow,
 $Ra_T = 1.53 \times 10^7$, $Pe = 4.63$, $Pr = .646$, $Le = .618$

are effective for damping convection. Also, in accordance to our scaling, since the height is fixed, the Rayleigh number does not change for the parametric variation approaching a vertical narrow cavity. This scaling shows conflicting trends between the solution and the magnitude of the Rayleigh number. Though the magnitude of the Rayleigh number indicates that we should be in a convectively dominated regime, the solution shows that the flow field becomes stable as the aspect ratio increases. In order to remediate this conflict, we hypothesize that the proper characteristic length should be the smallest dimension for cavities that are rectangular. In agreement with this hypothesis is the parametric variation to approach the horizontal narrow cavity. Note that in this case, since the dimension that is being varied, H , is the one used as characteristic length to scale the equations, the proper trend in the threshold of the Rayleigh number is reflected as the aspect ratio decreases. As we approach a narrow horizontal cavity there is a much faster change in the characteristic velocity. The results also show that the velocity tends to be higher for narrow horizontal cavities than for vertical ones, this is due to stronger wall effects for the vertical narrow cavity.

4. Dynamics of Flow Field At Fixed Point

In this section we analyze the four regions on the bifurcation diagram in Figure 2 from a dynamical systems perspective. For each region we analyze the time histories of the flow field and the scalar fields, the phase space trajectories of the flow field, and its

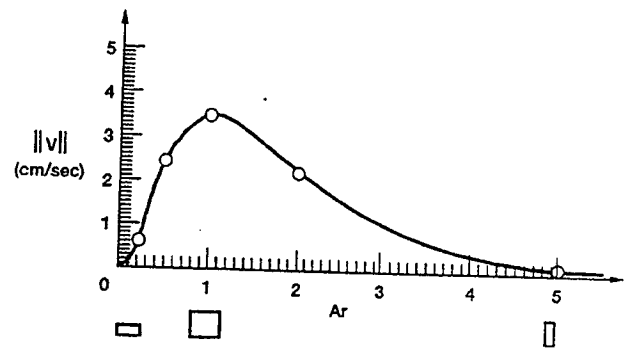


Figure 6. Effect of the aspect ratio

TABLE 2 - EFFECT OF ASPECT RATIO

Case	ϵ	Ar	Ra_T
20	1	1/5	2.13×10^3
21	1	1/2	3.32×10^4
22	1	1	2.66×10^5
23	1	2	2.66×10^5
24	1	5	2.66×10^5

power spectra. The phase space trajectory is obtained by plotting one component of the flow field versus the other. The power spectrum is evaluated using the Cooley-Tukey algorithm^{17, 18} and a Hanning window is used for filtering. The power spectrum for a variable, say χ , is estimated using Fast Fourier Transforms, from

$$\bar{P}_x(f) = \frac{1}{R} \left| \int_0^R \chi(t) e^{-j2\pi ft} dt \right|^2 \quad (12)$$

$$P_x(f) = W_S(f) * \bar{P}_x(f) \quad (13)$$

R is the finite time duration of the data, $\bar{P}_x(f)$ is the estimated power spectrum, and $W_S(f)$ is a spectral window for smoothing. The resulting smooth spectral estimate $P_x(f)$ is obtained from the convolution relationship in equation 13.

In order to select the best point in the flow field to display the dynamics, we plotted a set of points selected from various regions in the cavity. Regardless of the point selected, the results were similar, though they differed in amplitude. For each data set we used 5000 points. This required excessive data storage, for example one data set for our grid size (60x60) is on the order of 800 megabytes. In addition, a large number of CPU hours (depending on the machine, 30-100 hours on the average per case) is also necessary for computing the asymptotic behaviors of these flows. In some cases, because of resources, we were forced to be conservative.

4.1 Qualitative Bifurcation and Stability Analysis

Before delving into the results, we present qualitatively an explanation of the local bifurcation for the exchange of stability of the results in Figure 2. According to the literature on bifurcation and stability theory, if an infinite dimensional problem (set of coupled partial differential equations such as this problem) is approximated via truncation, it is possible to reduce the problem to a finite dimensional space (set of coupled ordinary differential equations). Given this step, one considers for argument sake an autonomous set of initial value ordinary differential equations,

$$\dot{Z} = f(Z, \Lambda) \quad (14)$$

$$Z(0) = \eta \text{ for } t \geq 0$$

where Z is a vector denoting the independent variables, \dot{Z} is its change with respect to time, Λ as before is a vector space containing n parameters, η is its initial or stationary condition. In accordance with the constraints in our problem, let $\Lambda = Ra_T$, this reduces the parametric dependence to a single parameter. The solution to the above set of equations yields a family of flow lines or trajectories. The basic question is whether or not the trajectory of Z remains near the neighborhood $f(Z, Ra_T) = 0$ for a given Ra_T as $t \rightarrow \infty$. If the trajectory of Z remains bounded in the neighborhood where $f(Z, Ra_T) = 0$ then the system is stable, and if Z grows or becomes unbounded then the system is unstable to the given state. Thus, it is necessary to investigate the set

$$f(Z, Ra_T) = 0 \quad (15)$$

to find the stationary or equilibrium points. The solution of this set of equations yield the stationary points,

$$(Z_1^*, Z_2^*, \dots, Z_n^*)$$

n corresponds to the dimension of the vector space. The next question as to whether or not the trajectory of the system remains in the neighborhood of these points, requires the solution of equation (14) near the points. This is accomplished by expanding f near the stationary points using a Taylor's series expansion. Dropping the parameter Ra_T for simplification and using component notation, the equations become

$$\dot{Z}_i = f_i(Z_1, Z_2, \dots, Z_n) \quad (16)$$

where,

$$f_i(Z_1, Z_2, \dots, Z_n) = f_i(Z_1^*, Z_2^*, \dots, Z_n^*) + \frac{\partial f_i}{\partial Z_1^*}(Z_1^*, Z_2^*, \dots, Z_n^*)(Z_1 - Z_1^*) +$$

$$\frac{\partial f_i}{\partial Z_2^*}(Z_1^*, Z_2^*, \dots, Z_n^*)(Z_2 - Z_2^*) + \dots$$

$$\frac{\partial f_i}{\partial Z_n^*}(Z_1^*, Z_2^*, \dots, Z_n^*)(Z_n - Z_n^*) + \text{higher order terms}$$

$$i = 1, 2, \dots, n$$

Then the local bifurcation of the system may be approximated by a first order approximation which indicates the degree to which the system deviates from its stationary values. This is represented by the vector,

$$\Phi_i(t) \approx Z_i(t) - Z_i^* \quad i = 1, 2, \dots, n \quad (17)$$

Then the linearized system in vector notation becomes

$$\dot{\Phi} = J^* \Phi \quad (18)$$

where

$$J^* = \frac{\partial f}{\partial Z}(Z^*)$$

$$J^* = \begin{bmatrix} \frac{\partial f_1}{\partial Z_1}(Z_1^*, Z_2^*, \dots, Z_n^*) & \frac{\partial f_1}{\partial Z_2}(Z_1^*, Z_2^*, \dots, Z_n^*) & \dots & \frac{\partial f_1}{\partial Z_n}(Z_1^*, Z_2^*, \dots, Z_n^*) \\ \frac{\partial f_2}{\partial Z_1}(Z_1^*, Z_2^*, \dots, Z_n^*) & \frac{\partial f_2}{\partial Z_2}(Z_1^*, Z_2^*, \dots, Z_n^*) & \dots & \frac{\partial f_2}{\partial Z_n}(Z_1^*, Z_2^*, \dots, Z_n^*) \\ \dots & \dots & \dots & \dots \\ \frac{\partial f_n}{\partial Z_1}(Z_1^*, Z_2^*, \dots, Z_n^*) & \frac{\partial f_n}{\partial Z_2}(Z_1^*, Z_2^*, \dots, Z_n^*) & \dots & \frac{\partial f_n}{\partial Z_n}(Z_1^*, Z_2^*, \dots, Z_n^*) \end{bmatrix}$$

J^* is the Jacobian matrix of the first order partial derivatives from the Taylor series expansion. The solution to equation (18) yields results concerning the local stability of the system. Since the system is linear, its solution may be obtained by inserting in equation (18) the hypothesis

$$\Phi_i(t) = e^{\sigma t} \xi_i \quad (19)$$

where σ is its eigenvalue, and ξ_i its eigenvector. Equation (18) becomes an eigenvalue problem as follows

$$(J^* - \sigma I) \xi = 0 \quad (20)$$

where I is the identity matrix. In order for equation (20) to have a nontrivial (linearly independent) solution it is necessary that $(\xi \neq 0)$, therefore $\sigma_1, \sigma_2, \dots, \sigma_n$ have to be the roots of the following characteristic equation

$$\det(J^* - \sigma I) = 0 \quad (21)$$

In the above equation, \det is the determinant. After evaluating the roots from equation (21), they may be inserted in equation (20) to find the eigenvectors ξ . However, the local stability is determined from the eigenvalues of equation (21). For our reduced case, the eigenvalues depend on Ra_T ,

$$\sigma_i(Ra_T) = \lambda_i(Ra_T) + j \kappa_i(Ra_T) \quad i = 1, 2, \dots, n \quad (22)$$

The general stability result, according to Liapunov¹⁹ may be stated as:

- (a) $\text{Re}(\sigma_i) < 0$ implies asymptotic stability for all i
- (b) $\text{Re}(\sigma_i) > 0$ implies instability for one or more i .

The behavior of the trajectories near the equilibrium or stationary points may be deduced from the values of σ_i . For example, consider a simple system with $i = 2$ which reduces the eigenvalue problem to the solution of quadratic roots. We will examine several cases in order to illustrate the qualitative behavior of trajectories⁶. From equation (22) consider the case when the eigenvalues (λ_1, λ_2) are real, i.e. $\kappa_i = 0$; two cases occur:

- (1) $\lambda_1, \lambda_2 > 0, \lambda_1 \neq \lambda_2$,

In this case the equilibrium or stable point Z^* is called a node. Two subcases result depending on the sign of λ . If $\lambda < 0$, the node is stable. However, if $\lambda > 0$, the node is unstable. This can be seen by examining $\lim_{t \rightarrow \infty} e^{\lambda t}$ for $\lambda > 0$ and $\lambda < 0$.

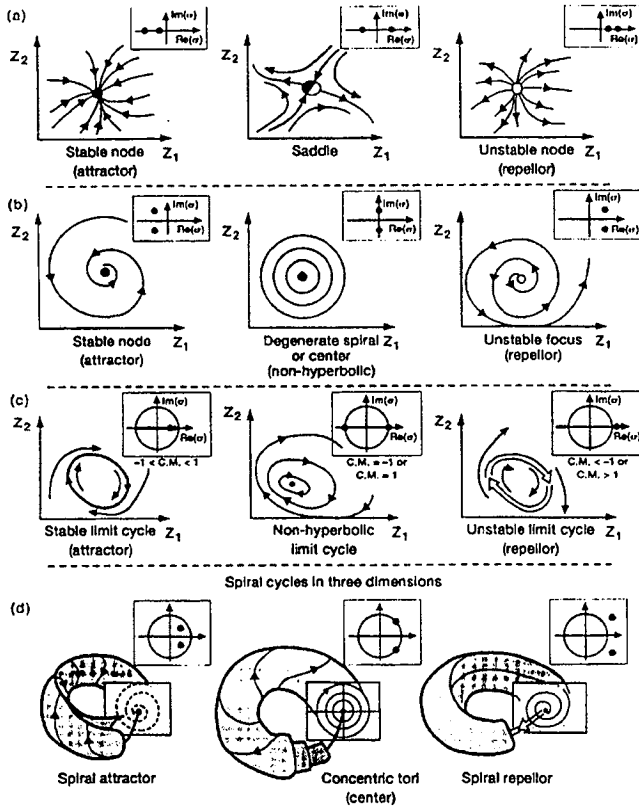


Figure 7. Qualitative behavior of state space trajectories with corresponding characteristic exponents and multipliers

(2) $\lambda_1 \lambda_2 < 0$,

In this case the stationary point is called a saddle point, which is always unstable. Typical trajectories for these cases are illustrated in Figure 7a.

For $\kappa_i \neq 0$, complex conjugates occur, and the trajectories near the equilibrium point resemble a spiral. For example, set

$$\sigma_1 = \lambda + j\kappa, \quad \sigma_2 = \lambda - j\kappa$$

For $\lambda > 0$, the corresponding equilibrium is called an unstable focus, and for $\lambda < 0$, a stable focus. Degenerate cases also occur, one example is for $\sigma_{1,2} = \pm j\kappa$, the corresponding trajectories are simply concentric circles as shown in Figure 7b. In addition note that since σ depends on Ra_T , the position and qualitative features of the stationary point varies as Ra_T changes. Thus there is a transition from one qualitative feature to another on the bifurcation diagram in Figure 2 as Ra_T increases.

This analysis yields the characteristic exponents as shown in Figure 8. Other characteristic trajectories such as a limit cycle may also occur. A limit cycle is a closed curve towards which the trajectory winds; it is the orbit of a periodic solution. This means that after some period \tilde{T} , the solution value remains the same,

$$Z(t + \tilde{T}) = Z(t)$$

The limit cycle may be stable or unstable depending on whether or not trajectories respectively approach or leave the neighborhood of the limit cycle. Examples of limit cycles are shown in Figure 7c. When $Z(t)$ is periodic, it is necessary to use Floquet theory to find the eigenvalues²⁰. These eigenvalues are called Floquet multipliers or characteristic multipliers (C.M.) as denoted on Figure 8. If the characteristic multipliers lie inside the circle the system is stable. When the characteristic multipliers cross the unit circle, the system becomes unstable. The mechanism by which stability is

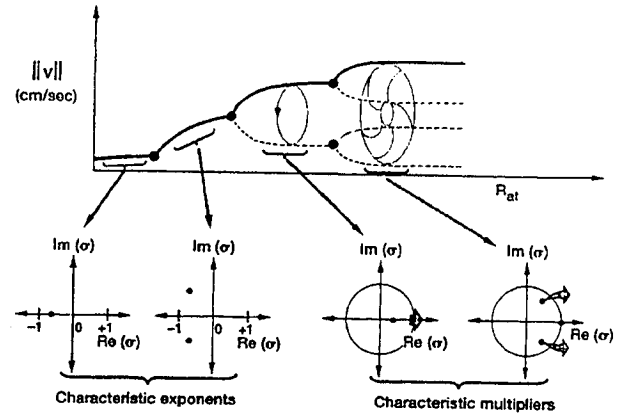


Figure 8. The mechanisms by which stability is lost

lost depends on how the characteristic exponents cross the axis of the real plane, likewise how the characteristic multipliers cross the unit circle.

Three dimensional spiral cycles can also occur as a result of losing stability. Illustration of spiral cycles are shown in Figure 7d after Abraham & Shaw²¹. These toroidal spiral cycles can result when there is a loss of stability from a limit cycle. If another frequency component arises, then a two frequency torus can occur as illustrated in Figure 8.

5. Quantitative Analysis of the Dynamical Behavior of the Flow Field

5.1 Region a

We now analyze in detail the dynamical behavior of the flow field for each region on the bifurcation diagram in Figure 2. We summarize the qualitative implications by which stability is lost in Figure 8. In the region where $0 < Ra_T < 9.0 \times 10^3$ the flow field is stable it is dominated by the advective-diffusive flux also known as the Stefan flow. The time history of the flow field as well as the scalar field are shown in Figure 9. These results indicate that the dynamics of the system approach a steady state behavior. This steady state behavior corresponds to a point attractor as shown by the corresponding location of its characteristic exponents, see Figure 8. Since there is no oscillation in the flow, the characteristic exponent lies on the negative real axis. As expected the concentration and temperature fields do not diffuse at the same rate, since $Le \neq 1$. This behavior is typical for any Rayleigh number in this range.

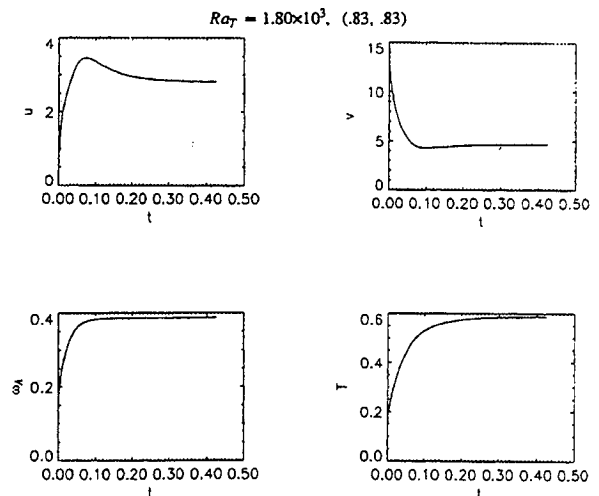


Figure 9. Dynamical behavior of a steady flow

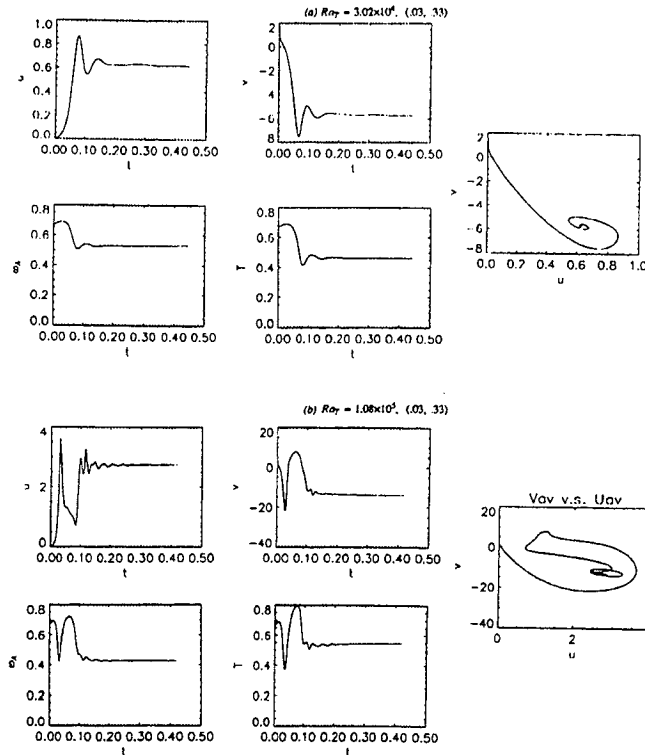


Figure 10. Spiral cycles

5.2 Region b

The first bifurcation from region *a* to *b* gives birth to a spiral; this is illustrated in Figure 10a by the phase space trajectory. The dynamics of the system indicate that the oscillations are quickly damped and the system approaches a point attractor. During this bifurcation the flow field selforganizes into two cells. This is similar to the Rayleigh-Benard system. Because of oscillations in the system the characteristic exponents are complex conjugates. As the Rayleigh number is increased (Figure 10b) these complex conjugates approach the real axis, see Figure 8. The behavior of the dynamics of the system change, it takes longer for the oscillations to decay. This is exemplified in the phase space trajectory by an increase in the number of spirals before it approaches its limit point. In this region which spans $9.3 \times 10^3 < Ra_T < 8.0 \times 10^4$, this course of event is representative.

5.3 Region c

Regions *a-b* demonstrated stationary states in which a dynamical equilibrium is approached. In contrast to the first bifurcation, the second bifurcation from *b* to *c* connects an equilibrium state to a periodic state. There is an exchange of stability from a stationary state to a periodic state. This bifurcation gives birth to a limit cycle; this is known as a primary Hopf bifurcation. The dynamical system characteristics of the flow field are shown in Figure 11. Near the Hopf bifurcation point, the asymptotic limit of the dynamics of the system shows very small oscillations, and a corresponding limit cycle in the phase space trajectory. The corresponding power spectrum shows a monofrequency response of approximately 0.2 Hz. As the Rayleigh number is increased, Figure 11b, the amplitude of the oscillations increase. For a different location of the flow field, Figure 11c, we show a limit cycle with a corresponding power increase in the power spectrum. However, the frequency response of the flow field remains the same. Further increase in the Rayleigh number ($Ra_T = 6.10 \times 10^5$, Figure 12) of the system shows that its dynamics exhibit nonlinearity. This nonlinearity is indicated by integral multiples of the fundamental frequency in the power spectrum of the flow field. In Figure 12a and 12b we show the short and long time asymptotics of the flow field

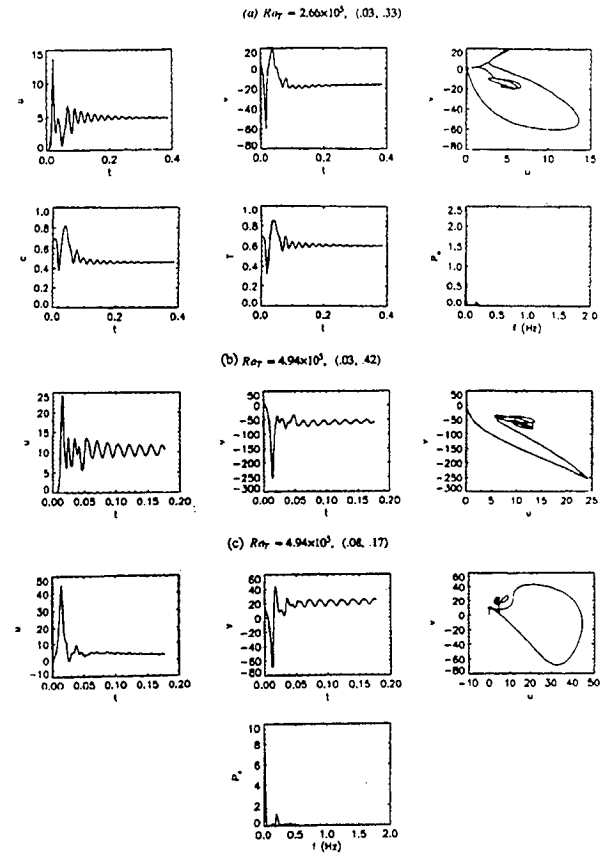


Figure 11. Dynamics in the neighborhood of a Hopf bifurcation

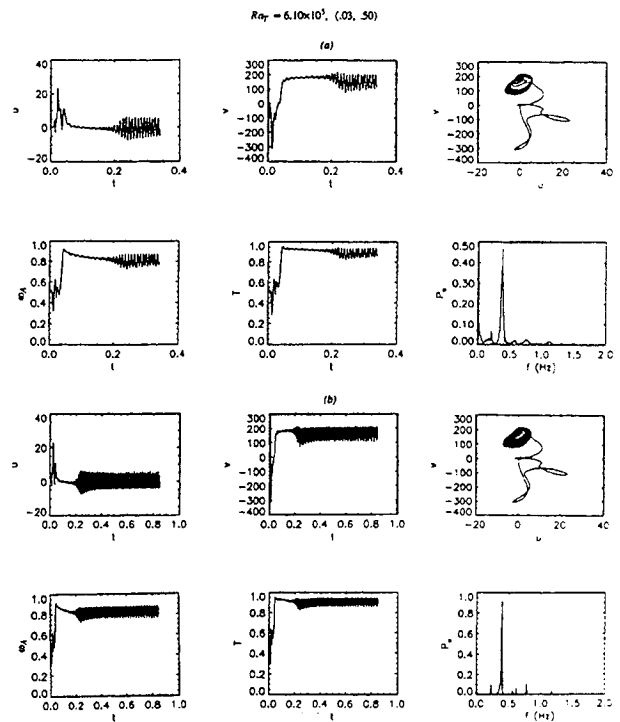


Figure 12. Periodic limit cycle with higher integral harmonics

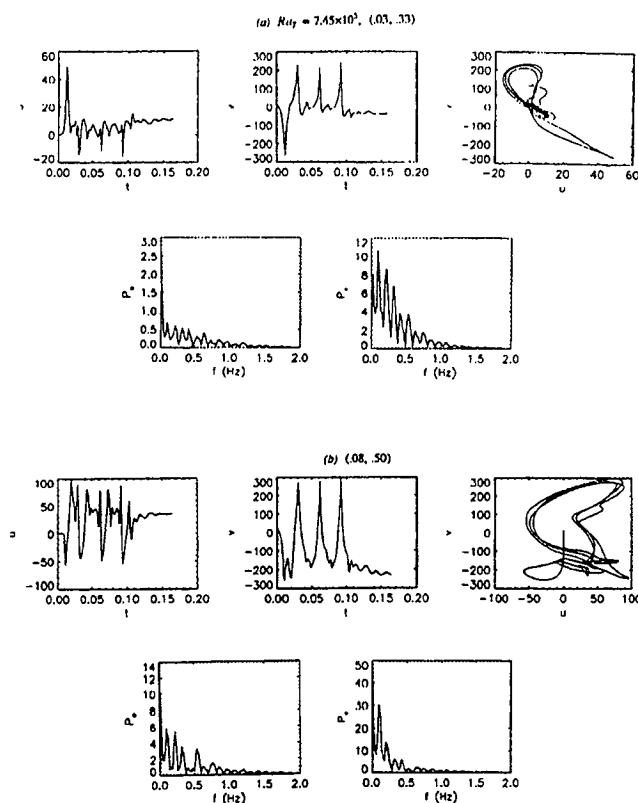


Figure 13. Transition to a quasi-periodic flow

respectively at the same point. Note that we obtain basically the same results, however 12b shows sharper resolution of the frequencies in the power spectrum. In this region we have a stable limit cycle; its corresponding characteristic multiplier is shown in Figure 8. Its location is on the real axis inside the circle. This region spans the range $8.0 \times 10^4 < Ra_T < 7.0 \times 10^5$.

5.4 Region d

In the bifurcation from region c to d, there is an exchange of stability from stable to unstable oscillation. The dynamical system characteristics are shown in Figure 13. In this sequence of events, the power spectra show the occurrence of an incommensurate frequency. The frequency ratio of this new component to the prior frequency forms an irrational ratio. This indicates a quasi-periodic state. The phase space shows the increase in complexity of the dynamics. Varying the location in the flow field, 13b, tells basically the same story. Note that the amplitude of the flow field increases dramatically in comparison to the case in Figure 12. The mechanisms of exchange of stability are illustrated in Figure 8; in this case the bifurcation gives rise to complex conjugate multipliers. Stability is lost through crossing the unit circle through the positive real components of the eigenvalues. This corresponds to a bifurcation to a two frequency torus which is also known as a secondary Hopf bifurcation. This bifurcation to a two frequency torus is one of the routes to chaos, which has been postulated by Newhouse, Ruelle, and Takens⁹.

In this region of operation, a slight change in the parameters of the system can result in unpredictable behavior of the future of the dynamical system. This is illustrated in Figure 14; for an increase in Rayleigh number, the system transitions to chaos. This is indicated by a broadband response in the power spectrum, 14a, and a thick chaotic limit set in the phase space trajectory. This thick chaotic limit set indicates that the future of the system is unpredictable. The precise location of a point cannot readily be discerned. Note that the concentration and temperature fields do not exhibit the same response as the flow field; this is due to

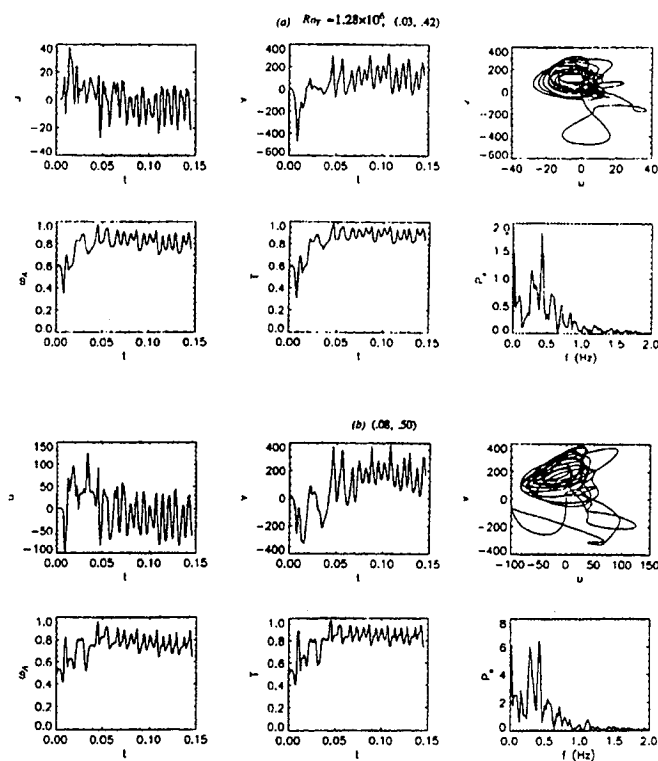


Figure 14. Transition to chaos

different dissipative mechanisms. Another location in the flow field, 14b, shows similar trends.

Subtleties in the dynamics of the flow field in the chaotic region as the Rayleigh number increases are shown in Figures 15, 16, and 17. As the Rayleigh number is increased, the response of the flow field shows an increase in amplitude. This is evident from a comparison between Figure 14a and Figure 15a. The power spectra exhibit a broadband distribution with more power concentrated at the low frequency region. At different location in the flow field, there is variance in the phase space trajectory, however the underlying feature of a thick chaotic limit set is preserved. These trends continue as the Rayleigh number increases, Figures 16 and 17. Note that for the highest Rayleigh number, Figure 17b, the phase space trajectory shows that the density of the thick chaotic limit set increases, which emphasizes the underlying future unpredictability of chaotic systems.

6. Applications to Crystal Growth

We have related the physics of the physical vapor transport process to actual laboratory practices by the experimentalists in terms of the parametric space of the system. For physical vapor transport with the presence of impurities, there occur 5 independent variables represented by our parametric space $\Lambda = \Lambda(Ra_T, Ar, Pe, Pr, Le)$. Our interest in the growth of large bulk single crystals ($Ar=1$) for a specific material (mercurous chloride) with a predetermined impurity content has reduced the parametric space to a single variable, $\Lambda = \Lambda(Ra_T)$. This implies that the process is controlled by varying the temperature difference between source and sink (ΔT). Thus a bifurcation diagram that can serve as a road map to an experimentalist is constructed. Its usefulness lies in its succinct representation of the dynamical characteristics of the process. We have shown four basic regions for a Rayleigh number range that covers low gravity to actual ground based conditions. It has been shown²² that high quality crystal growth can be obtained from low Rayleigh number growth conditions. This is because the growth of high quality single crystals requires steady

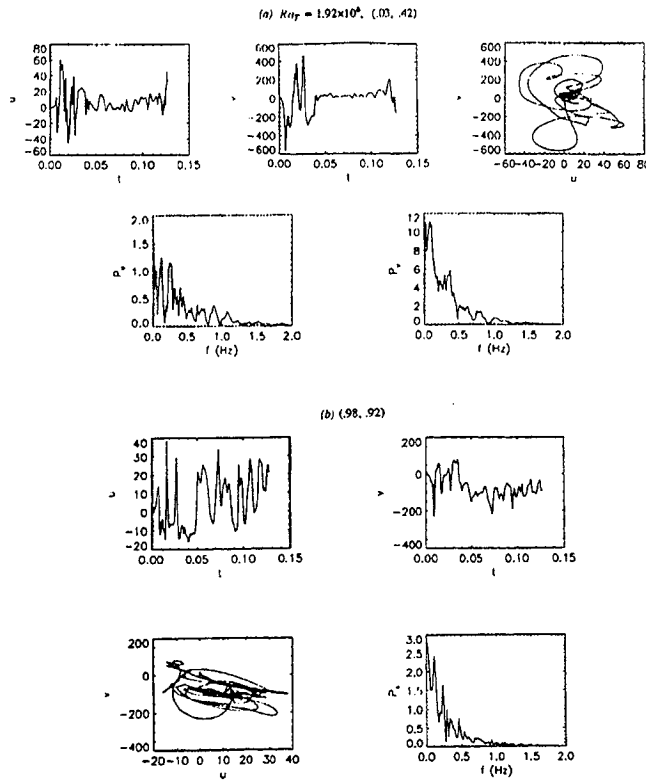


Figure 15. Dynamics in the chaotic region for $Ra_T = 1.92 \times 10^6$

transport of heat and mass. In this regard, the lower Rayleigh number range should provide the best growth conditions.

In terms of our bifurcation diagram, region *a* is the best parametric range to grow crystals ($0 < Ra_T < 9.0 \times 10^3$). Unfortunately for growth of large bulk single crystals it is not possible to obtain this parametric range in ground based laboratory conditions. This is possible only under low gravity conditions. The next range to grow crystals lies in region *b* ($9.0 \times 10^3 < Ra_T < 8.0 \times 10^4$). In this range it is also possible, under very careful experimental conditions, to grow high quality crystals. By careful experimental conditions, we mean that the furnace facility has to be able to be tuned appropriately to obtain ΔT as small as possible. This is not always possible given the limits associated with controlling temperatures in furnaces. However, if this is possible, even though flow oscillations occur in this parametric range, they decay eventually. And crystals can be grown under steady conditions, however the start-up of the process which involves nucleation events should proceed with caution. It is necessary to allow enough time for the system to settle to a steady state condition.

Beyond region *b*, the dynamics show that the process never reaches a steady state condition. Thus crystals grown under these conditions will show poor quality because of the fluctuations in the field variables which indicate unsteady heat and mass transport. Unfortunately under most ground base conditions the parametric range of region *c* is the most readily achievable condition obtained in a given furnace. However, as we pointed out, increasing or decreasing the aspect ratio is another parameter through which the dynamical characteristics can be changed. For argument sake, if we increase the aspect ratio and reconstruct the bifurcation diagram, we would effectively shift all bifurcation points to the right. This would give the experimentalist greater control of the process. A growth condition occurring in region *c* would be shifted to region *b*, and so on, where high quality crystal growth could potentially be carried out. However, we must emphasize that low gravity conditions are very effective for obtaining growth conditions in region *a*.

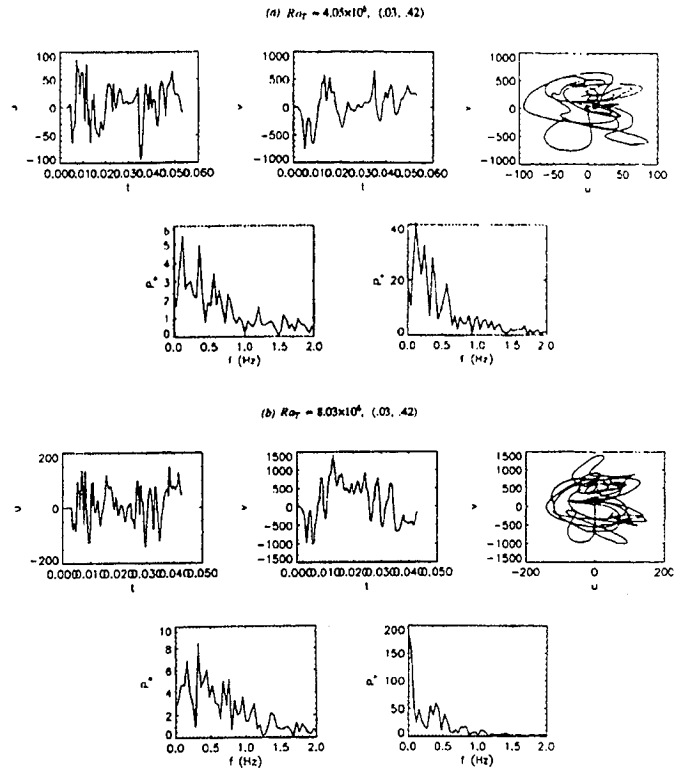


Figure 16. Dynamics in the chaotic region for $Ra_T = 4.05 \times 10^6$, and $Ra_T = 8.03 \times 10^6$

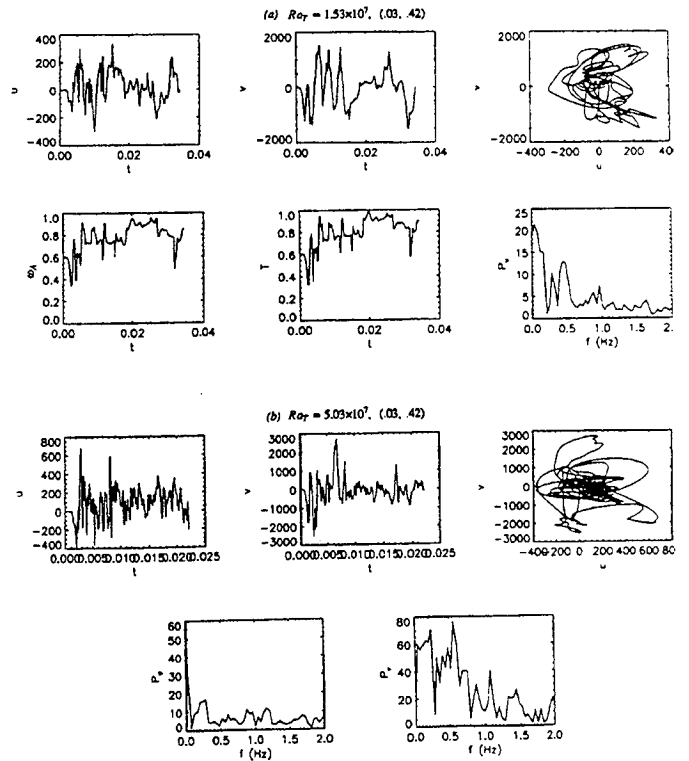


Figure 17. Dynamics in the chaotic region for $Ra_T = 1.53 \times 10^7$, and $Ra_T = 5.03 \times 10^7$

7. Summary and Conclusions

We have studied numerically the dynamical characteristics of flow field structures and its route to chaos in the physical vapor transport process. We showed that five independent parameters quantify the process. For a specific experimental system, we were able to reduce the number of parameters to a single important one, the Rayleigh number. To obtain a global picture of the process we constructed a bifurcation diagram and showed its distinct bifurcation sequence on its route to chaos. We explained qualitatively the mechanism of exchange of stability for each bifurcation event employing ideas from bifurcation and stability analysis. Each region in the bifurcation diagram was quantified through its time histories, phase space trajectories, and power spectra.

We show that four regions with distinct flow field structures occur. These structures occur through selforganization of the flow field. During the transition from one region to another, three distinct bifurcation events occur. The flow field structure transitions from a unidirectional advective-diffusive flow ($0 < Ra_T < 9.0 \times 10^3$) to two cells ($9.0 \times 10^3 < Ra_T < 8.0 \times 10^4$), subsequently to four cells ($8.0 \times 10^4 < Ra_T < 7.0 \times 10^5$), and finally six cells, ($7.0 \times 10^5 < Ra_T \leq 5.03 \times 10^7$). During each bifurcation sequence there is an exchange of stability from one type of dynamical behavior to another. The first bifurcation event gives birth to a stable spiral in which a point attractor is approached. In the second bifurcation there is an exchange of stability from a stationary state to a periodic limit cycle. This is called a standard Hopf bifurcation. In the third bifurcation there is an exchange of stability from stable to unstable oscillation. In terms of trajectories this corresponds to an exchange of stability from a periodic limit cycle to a two frequency torus. This unstable oscillation introduces an incommensurate frequency which gives birth to the two frequency torus. This route to chaos via torus bifurcation has been proposed by Newhouse, Ruelle, and Takens.

In so far as crystal quality is affected by the convective level, it is important to know the convective region that one is operating. In this regard, a bifurcation diagram is very useful to an experimentalist. Decreasing or increasing the aspect ratio is very effective for damping convection and achieving steady growth conditions. However, if one is constrained to grow large bulk single crystals, the bifurcation diagram indicates that $0 < Ra_T < 8.0 \times 10^3$ is the best region for crystal growth. For the cavity size considered, this can only be achieved under microgravity conditions.

8. Acknowledgment

The support of NASA Code UG Microgravity Science and Applications Division is gratefully acknowledged. Computational hardware support and graphics from R. L. Gaug and D. A. Thompson are also acknowledged.

9. Nomenclature

Ar	aspect ratio (H/L)
\bar{D}_{AB}	molecular mass diffusion coefficient
f	function
\bar{g}	acceleration of gravity
g_0	acceleration of gravity on earth
H	cavity height
Im	imaginary number
j	imaginary number
\hat{j}	unit vector in vertical direction
J^i	Jacobian of matrix
L	cavity width
Le	Lewis number
M	molecular weight
p	hydrodynamic pressure
P	partial pressure
P_x	power spectrum of variable x
Pe	Peclet number based on mass diffusion
Pr	Prandtl number
R	time duration of data
Ra_T	thermal Rayleigh number
Re	real number

t	dimensionless time
T	dimensionless temperature
\bar{t}	period
T_i	characteristic time (H^2/α)
u, v	dimensionless velocity in x and y directions ($u^*/U_c, v^*/U_c$)
U_c	characteristic velocity based on convection (α/H)
U_o	characteristic velocity based on the advective-diffusive flux
x, y	dimensionless horizontal and vertical directions ($x^*/L, y^*/H$)
W_s	spectral window
Z	vector denoting independent variable
\forall	for all

Greek characters

Γ	boundary of cavity
Λ	parameter space
α	thermal expansion coefficient
β	thermal expansivity
Δ	difference
γ	solatal expansivity
ϵ	ratio denoting reduction in acceleration of gravity
μ	dynamic viscosity
ν	kinematic viscosity
ω	mass fraction
Ψ	dimensionless stream function ($\Psi^*/U_c H$)
∇	gradient in x and y directions
ρ	density
σ	eigenvalue
ξ	eigenvector
∇^2	Laplacian in two directions
ζ	dimensionless vorticity ($\zeta^* H/U_c$)

Subscripts

A, B	denote components
c	crystal
s	source
T	total

Superscripts

*	dimensional quantity
-	average quantity
s	stationary value

10. References

1. Ebeling, W., and Y.L. Klimontovich, 1984. *Selforganization and Turbulence in Liquids*. Teubner-Texte zur Physik, pp 5-18.
2. Arroyo, M.P., and J.M. Saviron, 1992. "Rayleigh-Benard Convection in a Small Box: Spatial Features and Thermal Dependence of the Velocity Field," *Journal of Fluid Mechanics*, 235:325-348.
3. Mukutmoni, D. and K.T. Yang, 1992. "Wavenumber selection for Rayleigh-Benard Convection in a Small Aspect Ratio Box," *International Journal of Heat and Mass Transfer*, No. 9, 35:2145-2159.
4. Lorenz, E.N., 1962. "Deterministic Nonperiodic Flow," *Journal of The Atmospheric Sciences*, 20:130-141.
5. Saltzman, B., 1962. "Finite Amplitude Free Convection as an Initial Value Problem -I," *Journal of The Atmospheric Sciences*, 19:329-341.
6. Seydel, R., 1988. *From Equilibrium To Chaos: Practical Bifurcation and Stability Analysis*. Elsevier Science Publishing Co., Inc., pp 109-125.
7. Kubicek, M. and M. Marek, 1983. *Computational Methods in Bifurcation Theory and Dissipative Structures*. Springer-Verlag New York, Inc., pp 36-101, 175-181.

8. Velarde, M.G., 1981. "Steady States, Limit Cycles and The Onset of Turbulence. A Few Model Calculations and Exercises," In *Nonlinear Phenomena at Phase Transitions and Instabilities* (ed. T. Riste), pp 205-247.
9. Newhouse, S., D. Ruelle, and F. Takens, 1978. "Occurrence of Strange Axiom A Attractors Near Quasi-Periodic Flows on T^m , $m \geq 3$," *Communications in Mathematical Physics*, 64:35-40.
10. Conder, K., J. Przyliski, and J. Laskowski, 1986. "Vapor Transport Rate of HgI_2 in the Presence of Inert Gas," *Journal of Crystal Growth*, 74:416-424.
11. Faktor, M.M., and Garret, I., 1974. *Growth of Crystals from The Vapour*. John Wiley and Sons, Inc., pp. 109-120.
12. Bird, R.B., Stewart, W.E., and Lightfoot E.N., 1960. *Transport Phenomena*. John Wiley and Sons, Inc., pp. 19-26, 253-260, 495-501, 508-513.
13. Westphal, G.H., and Rosenberger, F., 1978. "On Diffusive-Advective Interfacial Mass Transfer." *Journal of Crystal Growth*, 43: 687-693.
14. Rosenberger, F., and G. Muller, 1983. "Interfacial Transport in Crystal Growth, A Parametric Comparison of Convective Effects," *Journal of Crystal Growth*, 65:91-104.
15. Duval, W.M.B., 1992. "Convective Effects During The Physical Vapor Transport Process - I: Thermal Convection." *Journal of Materials Processing and Manufacturing Science*, 1:83-104.
16. Shvartsblat, D.L., 1969. "Steady Convective Motions in a Plane Horizontal Fluid Layer With Permeable Boundaries." *Izv. AN SSSR. Mekhanika Zhidkosti i Gaza*, Vol. 4, No. 5: 84-90.
17. Cooley, J.W., and Tukey, J.W., 1965. "An Algorithm for The Machine Calculation of Complex Fourier Series." *Mathematics of Computations*, 19: 297-301.
18. Brigham, E.O., 1988. *The Fast Fourier Transform and Its Applications*, Prentice-Hall, Englewood Cliffs, New Jersey, pp. 131-166.
19. Liapunov, A.M., 1966. *Stability of Motion*. New York: Academic Press, pp. 13-127.
20. Ioos, G., and D.D. Joseph, 1981. *Elementary Stability and Bifurcation Theory*. New York: Springer, pp. 123-156.
21. Abraham, R.H., and C.D. Shaw, 1983. *Dynamics the Geometry of Behavior part two: Chaotic Behavior*. Aerial Press, Inc. pp 31-63.
22. Singh, N.B., and Duval, W.M.B., 1991. "Growth Kinetics of Physical Vapor Transport Processes: Crystal Growth of The Optoelectronic Material Mercurous Chloride." NASA Technical Memorandum 103788.

